

# Overcoming Barriers to Dynamic Phase-Only Modulation in Transmissive Metasurfaces via Diffraction Control

Juyoung Kim,<sup>||</sup> Ruzan Sokhoyan,<sup>||</sup> Minkyoon Yi, Sangjun Han, Harry A. Atwater,<sup>\*</sup> and Min Seok Jang<sup>\*</sup>



Cite This: *ACS Nano* 2026, 20, 6622–6631



Read Online

ACCESS |



Metrics & More



Article Recommendations



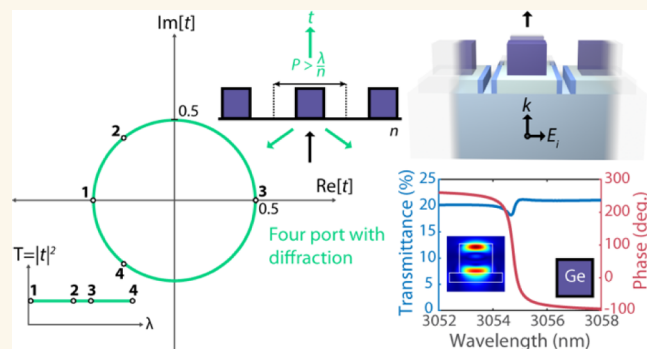
Supporting Information

**ABSTRACT:** Active photonic systems comprising arrays of active metasurfaces—arrays of tunable resonators—offer dynamic wavefront control at subwavelength scales. Transmissive metasurfaces are an essential requirement in cascaded arrays of metasurfaces and enable integration with chip-scale light sources and detectors. However, most existing active phase control metasurface designs are reflective due to fundamental limitations in single-resonance transmissive architectures, which typically exhibit a transmission null at resonance and restrict transmitted phase shifts to 0–180°. We report an approach to overcome these constraints by introducing additional diffraction ports in reflection while maintaining a single transmission port. This configuration enables continuous 0–360° phase tuning in transmission using a single resonance while avoiding the transmission zero. Moreover, we analytically demonstrate using temporal coupled-mode theory that this approach supports a spectrally flat transmission amplitude across the entire phase range—an effect previously observed only in multiresonant (Kerker-type) systems. Unlike those, our design allows dynamic phase control with a single resonance and a constant transmission. To validate our theory, we present proof-of-concept active metasurfaces using lithium niobate as the tunable material. Two designs are explored via full-wave simulations: one using high-Q germanium Mie resonators at 3 μm, achieving ~250° tunable phase shift with constant transmission amplitude ~0.45; and another using silicon resonators at telecom wavelengths, demonstrating ~300° phase shift with amplitude ~0.4. Both approaches approach the theoretical transmission bound of 0.5. Our approach enables compact, dynamically tunable transmissive metasurfaces with near-ideal phase and amplitude characteristics, paving the way for integrated, reconfigurable metasurfaces.

**KEYWORDS:** phase modulation, active metasurfaces, diffraction, transmission zero, Fano curve, phase-only control

Intensive research has advanced our understanding of nanophotonic light–matter interactions, and we are entering an era where nanophotonic principles are having an ever-increasing impact in imaging and computation systems for applications such as range-finding,<sup>1,2</sup> image processing,<sup>3</sup> augmented reality,<sup>4</sup> and dynamic holography.<sup>5</sup> Despite this progress, a number of outstanding challenges remain, one of which is to achieve comprehensive control of wavefront manipulation in space and time in active systems. Achieving this requires delicate real-time control over how electromagnetic waves strongly interact with arrays of scatterers through a tuning parameter that can be controlled on-demand, which has led to intensive research in the properties of optical metasurfaces.<sup>6–12</sup> Metasurfaces present a vast design space, which has recently spurred remarkable advances in dynamic wavefront shaping using various active modulation methods,<sup>11–15</sup> enabling active phase control of scattered waves.<sup>10,15–17</sup>

Dynamically controlling the phase of the scattered waves is done by actively tailoring the scattering environment, which, in turn, alters the wave interaction and therefore the scattered



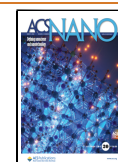
phase. In active metasurfaces, components that can be modulated include the structural geometry and constitutive parameters of the materials used, such as complex permittivity. Because of physical limits to the magnitude of achievable real-time changes that can be imparted to the metasurface, researchers have opted to use photonic resonances to enhance modulation owing to the rapid changes in scattered phase at resonance with respect to the input frequency.<sup>10,15,17</sup> Incident light excites the resonance by oscillating charges and currents, which emit waves of their own; the corresponding phase difference is influenced by the frequency of the incident wave relative to the resonance frequency and the resonant spectral line width. The resonance frequency and the line width are in

**Received:** August 4, 2025

**Revised:** January 28, 2026

**Accepted:** January 29, 2026

**Published:** February 11, 2026



turn determined by the structural and material properties of the metasurface.

One complication that comes with harnessing resonant phenomena is that the amplitude and phase responses are coupled to one another. Phase-only control, where the amplitude remains constant while the phase is modulated, is often preferred in wavefront engineering applications. According to the Huygens principle, every point on a wavefront acts as a source of secondary wavelets that propagate forward. Thus, to generate clean, constructively interfering wavefronts, it is desirable to vary the phase without altering the amplitude.

An additional complexity arises from the fact that we are working with transmissive-type metasurfaces. When a wave scatters from a metasurface, it can be either reflected or transmitted, depending on the design. Reflective and transmissive metasurfaces each have their respective advantages and limitations; however, transmissive metasurfaces are particularly well-suited for stacking and compact on-chip applications—especially when monolithic integration with chip-scale light sources like photonic crystal surface emitting lasers (PCSELs) and vertical cavity surface emitting lasers (VCSELs) is desired.<sup>9,18,19</sup> However, achieving active phase-only modulation in transmission metasurfaces is more challenging because of the presence of two ports, one for the incident channel and one for the transmission channel, instead of having only one port, as in reflective setups. If one is only interested in reflection, breaking the vertical parity symmetry allows the metasurface to attain a full  $2\pi$  phase range.<sup>6,20–22</sup> In practice, this is done by inserting a reflecting mirror (usually gold) underneath the metasurface, which breaks the vertical parity symmetry and conveniently also cuts off the transmission channel, boosting the reflection intensity. Then, to attain phase-only control, it has been shown that overcoupling the resonance can result in large reflection amplitudes that are constant as the phase is varied.<sup>10</sup>

However, for transmissive metasurfaces, the presence of an extra port complicates matters. It has been mathematically shown that a lossless photonic system with two ports and a single resonance is bound to have a frequency near the resonance frequency at which the reflectance reaches unity,<sup>23</sup> which equates to having zero transmittance. Alongside the obvious concomitant drop in the transmission amplitude as the phase is varied, this transmission zero also constrains the range of the phase of the transmitted light to be  $\pi$  at best, heavily restricting the performance of dynamic phase modulation in transmissive metasurfaces. To circumvent this issue, researchers have used two overlapped resonances instead of one—by engineering the two resonances to destructively interfere in the reflection (incident) channel to form a Huygens metasurface.<sup>21,24–28</sup> However, this method is limited in active tuning schemes: a single active tuning parameter (such as the bias voltage) separates the two resonances beyond a specified tuning range, breaking the Kerker condition required to maintain the high transmission amplitude. This necessitates a secondary tuning parameter to maintain their overlap,<sup>29</sup> complicating the metasurface control architecture.

It is also worth noting that Pancharatnam–Berry (PB) phase (geometric-phase) metasurfaces<sup>30–32</sup> can provide high transmission/reflection efficiencies and a full  $0–2\pi$  phase range through rotation of the meta-atoms. However, because this phase mechanism fundamentally relies on the physical rotation of anisotropic elements, PB metasurfaces are not suitable for fully solid-state, real-time dynamic tuning.

Unidirectional guided resonances can also provide a full  $0–2\pi$  transmission phase variation in the spectral domain with near-unity transmission efficiency.<sup>33,34</sup> However, because the guided modes possess finite transverse momentum, these systems require non-normal incidence or transmission ports, which complicates their integration and stacking. Furthermore, being collective and nonlocal in nature, these modes must propagate across at least multiple unit cells for diffractive effects to manifest, which limits the achievable spatial resolution of the metasurface—particularly in applications involving subwavelength wavefront engineering. Also, placing these unidirectional guided resonant structures on a substrate significantly reduces their transmission efficiency.<sup>35</sup>

Here, we aim to achieve dynamic phase-only modulation in a transmission metasurface with a single resonance using a single tuning parameter. The formalism of temporal coupled mode theory (TCMT) is employed to geometrically illustrate the phenomenon of zero transmission in a two-port system with a single resonance in the complex transmission amplitude space. Next, we demonstrate how using additional diffraction ports can remove this restriction. Furthermore, by using the diffraction ports, we show that it is possible to achieve uniform transmission amplitude in the spectral domain while varying the phase through the  $0–2\pi$  range with a single resonance. We support our claim with a proof-of-concept metasurface and provide a general step-by-step methodology that can be used to achieve transmissive phase-only control in broader metasurface platforms. The analysis elucidates the role of each metasurface geometric parameter in achieving phase-only control. We also establish the theoretical upper bound for the transmission amplitude and discuss our approach to achieving a value close to the theoretical maximum.

Our proof-of-concept metasurface is composed of an array of high-index dielectric pillars that support high-Q Mie resonances. One of the high-Q resonances is then modulated with an electro-optically tunable lithium niobate (LN) pedestal slab, enabling dynamic control of the optical response under an applied bias. We demonstrate that the designed metasurface achieves a nearly constant complex transmission amplitude of 0.46, while the transmission phase varies continuously from  $0^\circ$  to  $360^\circ$  across the spectral domain. By incorporating indium tin oxide (ITO) electrodes into the design, we exploit the Pockels effect to dynamically modulate the refractive index of the LN. We provide two actively tunable configurations, one using germanium (Ge) as the dielectric pillars and the other using silicon (Si), to showcase the general applicability of our approach. In the Ge configuration, the complex transmission amplitude remains at approximately 0.45, while the transmission phase tunability spans  $0–250^\circ$  at  $\lambda \approx 3 \mu\text{m}$ . The Si case has a complex transmission amplitude at around 0.4 and exhibits a tunable phase range of  $0–300^\circ$  at telecommunication frequencies.

## RESULTS AND DISCUSSION

First, we use TCMT to understand the origin of the zero-transmission dip observed in two-port systems. The zero-transmission dip arises from Fano interference, where the continuum radiation and the resonant emission destructively interfere—a consequence of energy conservation and time-reversal symmetry. Previous work demonstrated this using an algebraic approach,<sup>23</sup> but here we adopt a geometric perspective, which offers insight suited to phase-only modulation. Using TCMT, for a general  $n$ -port system with

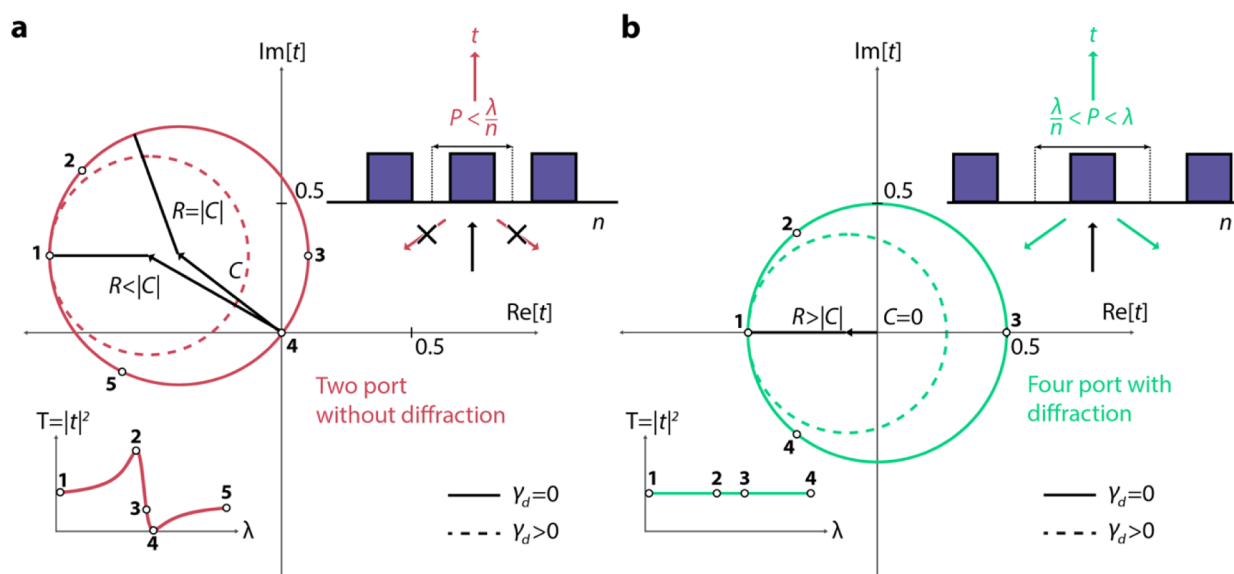


**Figure 1.** Limitations of a two-port, single-resonance system, and the potential full  $2\pi$  phase range in the transmission with a four-port system utilizing diffraction, Figure 1. (a) In a two-port system with a single resonance, the complex transmission amplitude is bound to go through the origin, preventing  $2\pi$  phase variation in the spectral domain. Here,  $\lambda/n$  denotes the wavelength inside the substrate of refractive index  $n$ , as illustrated in the upper-right inset. The numbered wavelengths correspond to 1 beginning of a resonance, or the “background” direct scattering parameter  $t_d$ ; 2, the furthest point from the origin in the complex transmission amplitude space, corresponding to the peak in the Fano spectrum in the transmission intensity; 3, the resonance wavelength; 4, the transmission zero; and 5, nearing the end of the resonance. Notice that with dissipative losses  $\gamma_d > 0$ , the transmission circle gets even smaller in radius, further decreasing the range of phase modulation. (b) In a four-port system with additional diffraction ports, one can judiciously change the direct scattering parameter  $t_d$  such that the complex transmission circle can be perfectly centered with a theoretical maximum of 0.5 for the radius. This allows for a phase-only  $2\pi$  phase modulation, with the wavelengths 1–4 all having the same distance from the origin (radius), leading to a flat transmission intensity. For the illustration of complex reflection circles, see the end of Supporting Information, Section 1.

a single resonance, the complex transmission amplitude is given by

$$t = t_d + t_r = t_d + \frac{id_1d_2}{(\omega - \omega_0) + i\gamma} = t_d + \frac{2i\sqrt{\gamma_1\gamma_2}}{(\omega - \omega_0) + i\gamma} \quad (1)$$

The derivation and additional details regarding TCMT are provided in Supporting Information, Section 1. The first complex-valued term,  $t_d$ , is the direct scattering parameter from the incident channel to the transmission channel and represents the portion of light that does not interact with the resonance. The second term,  $t_r(\omega)$ , represents the portion of radiation that is coupled to and then emitted by the resonance, where  $d_m = \sqrt{2\gamma_m}e^{i\theta_m}$  is the radiative coupling parameter for the  $m$ th port (with port 1 being the incidence port and port 2 being the transmission port),  $\omega_0$  is the resonance frequency, and  $\gamma = \sum_{m=1}^n \gamma_m + \gamma_d$  is the total decay rate of the resonance, defined as the sum of all radiative coupling ( $\gamma_m$ ) and dissipative decay ( $\gamma_d$ ) rates. The second equality, where we have taken  $\theta_{1,2} = 0$  comes from the following: since the port locations can be chosen arbitrarily, we have used the convention of placing the ports such that the radiative coupling values  $d_1$  and  $d_2$  are positive real, without loss of generality (see Supporting Information, Section 1).

Assuming the direct scattering parameter  $t_d$  is constant throughout the vicinity of the resonance frequency, it can be shown that the resonance term  $t_r(\omega)$  draws a circle on the complex transmission amplitude plane, with  $t_d$  pointing to the leftmost point on the circle (from the origin) and the resonance frequency ( $\omega = \omega_0$ ) corresponding to the rightmost

point (see Supporting Information, Section 1). This statement itself is quite astonishing, as the argument of the resonant term  $t_r(\omega)$  only ranges from 0 to  $\pi$ , which goes with the commonplace intuition of either resonating with the driving frequency or having a  $\pi$  phase lag relative to the driving frequency in resonance phenomena. However, if we also take into consideration the concomitant change in magnitude of  $t_r(\omega)$  as its phase evolves from 0 to  $\pi$ , we can see that the tip of the vector of  $t_r(\omega)$  draws a circle in the complex amplitude space (Supporting Information, Section 1). The nature of a full circle then allows for the possibility of  $0-2\pi$  phase variation in the spectral domain depending on where the center of the circle is with respect to the origin. The circle’s radius is given by  $R = \sqrt{\gamma_1\gamma_2}/\gamma$  and its center vector by  $C = R + t_d$  from eq 1. To determine whether the circle revolves around the origin, one can examine the sign of  $R - |C|$  (see Figure 1). If  $R > |C|$ , then the complex transmission amplitude circle revolves around the origin and, in principle, dynamic full  $2\pi$  phase modulation is achievable with a single control parameter. If  $R \leq |C|$ , the winding number around the origin cannot be one, and the circle does not permit complete  $2\pi$  phase modulation.

In a two-port, single-resonance system, it can be shown that from time-reversal symmetry, reciprocity, and energy conservation (Supporting Information, Section 1)

$$R^2 - |C|^2 = -2R \text{Re}[t_d] - |t_d|^2 = -\frac{\gamma_d}{\gamma} |t_d|^2 \leq 0 \quad (2)$$

where the radiative coupling strengths  $\gamma_i$ ’s are defined to be positive. From this, we can note that when there are zero dissipative losses ( $\gamma_d = 0$ ),  $R = |C|$  and the complex transmission amplitude circle is bound to cross through the

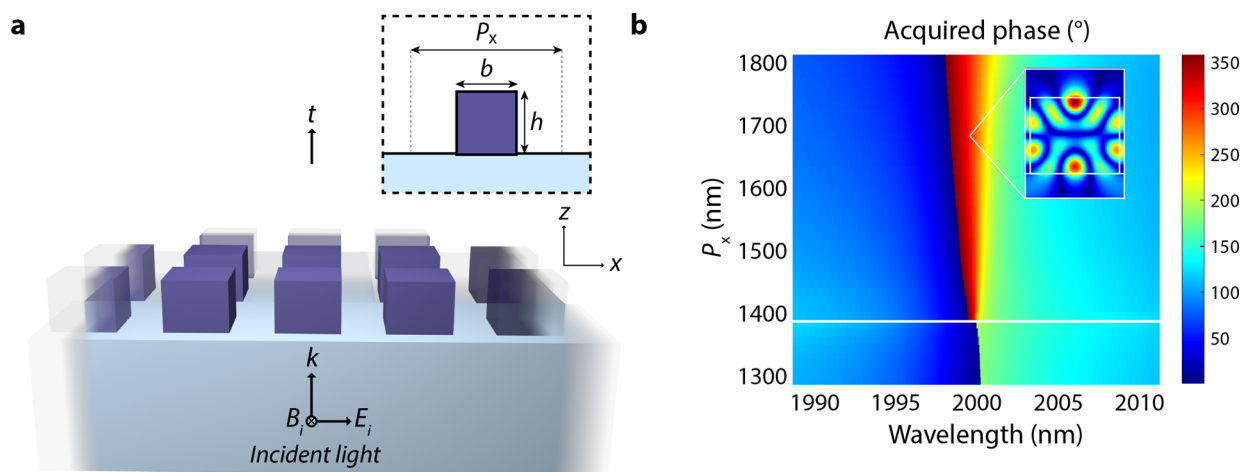


**Figure 2.** Phase of the transmitted light and its dependence on metasurface periodicity and diffraction, **Figure 2.** (a) A two-dimensional periodic metasurface with germanium pillars ( $n = 4$ ) on top of a silica substrate ( $n = 1.44$ ). (b) The phase of the transmitted light obtained through full wave simulations as the period in the  $x$ -direction  $P_x$  is tuned. The inset shows the electric field profile of the Mie resonance in the  $y$ - $z$  plane passing through the center of the pillar. The inner white box delineates the outline of the pillar. Once the  $P_x$  exceeds the threshold at which diffraction starts to occur in the substrate ( $P_x = \lambda/n_{\text{sub}} = 1388.9$  nm) for  $\lambda = 2000$  nm, the phase of the transmitted light is allowed to span the full  $360^\circ$  range. The dimensions for the pillar are height  $h = 999$  nm base and width  $b = 1167.7$  nm (square base area). The period in the  $y$  direction is fixed as  $P_y = 1328.6$  nm.

zero. When dissipative losses are introduced ( $\gamma_d > 0$ ),  $R$  shrinks due to the increase in the total decay rate,  $\gamma = \sum_{i=1}^n \gamma_i + \gamma_d$  with the “anchor” point  $t_d$  keeping the leftmost point on the circle fixed. This results in  $R < |C|$  (**Figure 1a**). The above underlines the limitation of reciprocal two-port single-resonance systems for active phase modulation—they are fundamentally incapable of providing  $2\pi$  phase modulation with a single control parameter. It should be noted that the derivation of the bound  $R \leq |C|$  presented in **Supporting Information**, Section 1, is valid for any combination of radiative and dissipative losses ( $\gamma_i$  and  $\gamma_d$ ). Consequently, variations in  $t_r$  arising from tuning the metasurface geometry, which effectively modifies  $\gamma_i$  and  $\gamma_d$ , do not affect the validity of the two-port constraint  $R \leq |C|$ .

This limitation can be overcome by increasing the number of ports. The underlying idea is as follows: the reason for the perfect cancellation in transmission is because  $|t_d| = |t_r(\omega)|$  at a certain  $\omega$  as the dynamic complex vector  $t_r(\omega)$  sweeps through a circle as a function of  $\omega$  ( $t_d$  assumed relatively constant). Therefore, if we could decrease  $|t_d|$  through adding more direct scattering terms  $\sum_i |\alpha_i|^2$  in the energy conservation equation  $|r_d|^2 + |t_d|^2 + \sum_i |\alpha_i|^2 = 1$  (compared to the two-port version of  $|r_d|^2 + |t_d|^2 = 1$ ), the perfect cancellation condition could be evaded. More specifically, if we consider a lossless two-port system with  $\arg[t_d] = \pi$ , or equivalently,  $t_d = -|t_d|$ , the constraint of **eq 2** enforces  $t_d = -2R$ . By increasing the number of ports,  $|t_d|$  can be decreased, resulting in  $R^2 - |C|^2 = |t_d|(2R - |t_d|) > 0$  from **eq 2**, meaning that the complex transmission amplitude circle encircles the origin while still satisfying reciprocity, time-reversal symmetry, and energy conservation. We note that the resonance circle can be perfectly centered (i.e.,  $C = 0$ ) when  $|t_d|$  is reduced to  $t_d = -R$ . If the complex transmission amplitude circle is centered close enough to the origin, then even the presence of moderate losses, which reduces  $R$  still does not change the winding number of 1 around the origin, making this topologically protected. In this work, we chose these additional ports to be diffraction channels as schematically illustrated in **Figure 1b**.

The theoretical upper bound for the radius of the resonance circle,  $R = \sqrt{\gamma_1 \gamma_2} / \gamma$ , is 0.5, as shown in **Supporting Information**, Section 1. The condition of  $R = 0.5$  can be achieved by equalizing the radiative couplings of the resonance to the incident and the transmission ports ( $\gamma_1 = \gamma_2$ ) and by suppressing the dissipative losses ( $\gamma_d = 0$ ) and the radiative couplings to the additional diffraction ports ( $\gamma_{i>2} = 0$ ).

Let us now illustrate with an example metasurface how the introduction of diffraction channels in reflection leads to an abrupt change in the transmission phase characteristics, i.e., transition from  $R = |C|$  to  $R > |C|$ . This metasurface is composed of an array of high-index Ge pillars ( $n_{\text{Ge}} = 4$ ) on a silica ( $n_{\text{silica}} = 1.44$ ) substrate and is illuminated at normal incidence by a linearly polarized plane wave originating from within the substrate, as shown in **Figure 2a**. The pillars support a higher-order Mie resonance, which, based on the field profile, corresponds to a dotriacontapole mode—also known as the 32-pole in the multipole expansion. It is worth noting that this mode has been previously studied, albeit in the context of arrays of Si resonators.<sup>36</sup> For additional field profiles, see **Supporting Information**, Section 2.

Diffraction of the reflected light within the silica substrate is introduced when the metasurface period in the  $x$ -direction,  $P_x$ , exceeds the threshold value  $P_0 = \lambda/n$ , where  $\lambda$  is the free-space wavelength and  $n$  is the refractive index of silica. As shown in **Figure 2b**, for subdiffraction periods ( $P_x < P_0$ ), the phase of the transmitted light exhibits an abrupt spectral variation, limited to a range of  $0$ – $180^\circ$ . Concurrently, a dip to zero in transmittance occurs at the resonance. This behavior is characteristic of the subdiffraction regime, where the condition  $R = |C|$  holds. However, once diffraction in reflection is introduced ( $P_x > P_0$ ), the phase of the transmitted light transitions to a smooth variation over the full range from  $0$  to  $2\pi$ , as illustrated in **Figure 2b**. Thus, introducing diffraction in reflection enables achieving the sought-after condition  $R > |C|$  for the transmitted light. Although our study focuses on the dotriacontapole resonance as an example, the described

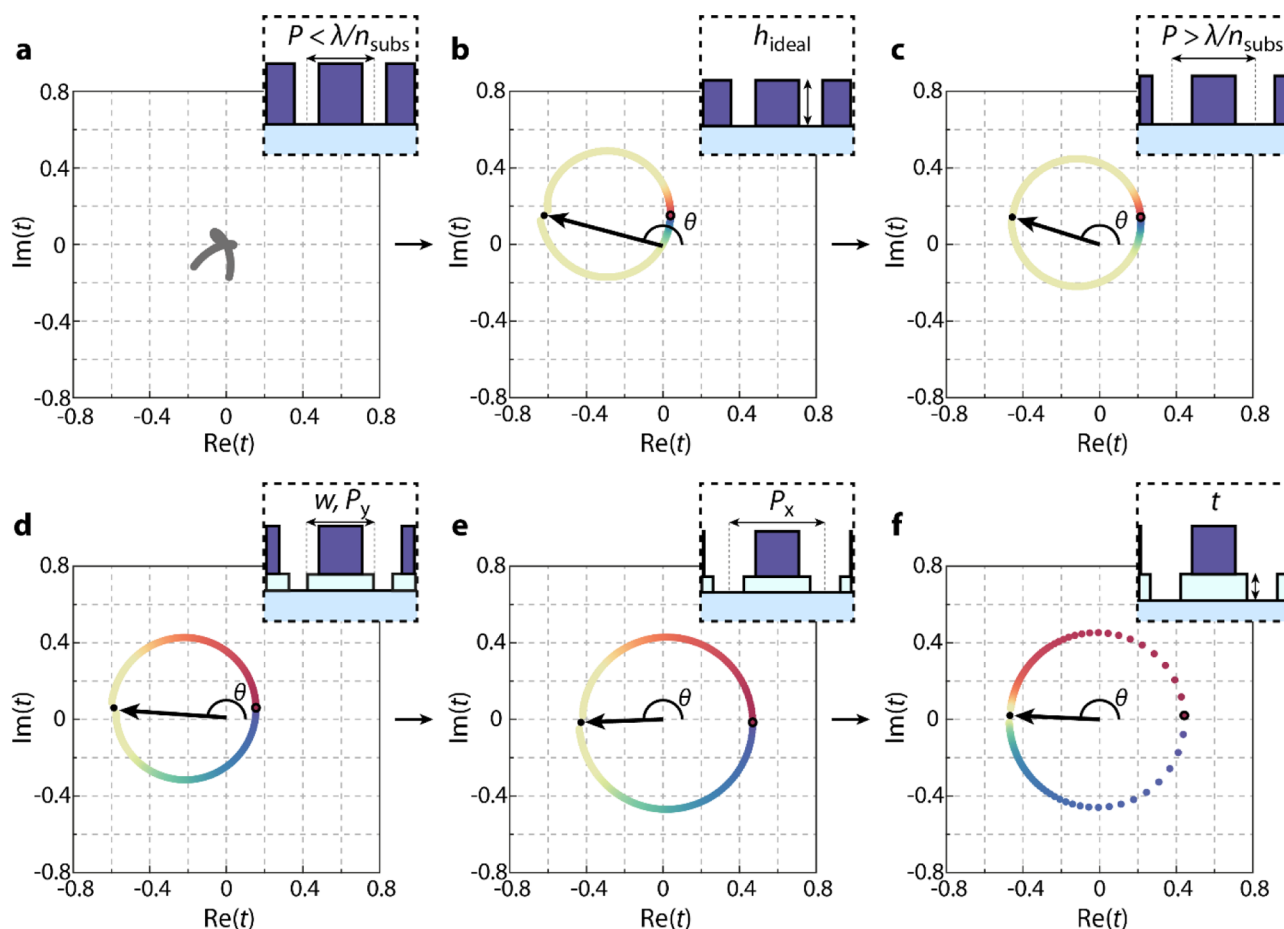


**Figure 3.** Progressive engineering of the complex transmission amplitude circle, Figure 3. (a) A periodic metasurface with pillars supporting three resonances that are in close spectral proximity. The dimensions of the pillars are 1175.5 nm  $\times$  1175.5 nm  $\times$  1502.0 nm (square base). Due to the subwavelength periodicity of  $P_x = P_y = 1387.1$  nm compared to the wavelength range of 2149.1–2163.0 nm (in the substrate:  $\lambda/n_{\text{sub}} = 1492.9$ –1502.1 nm) and the corresponding diffractionless nature, the complex transmission amplitude is bound to cross the origin near the vicinity of each of the resonance frequencies, resulting in three origin crossings (three resonances) that draw a ribbon-like shape on the complex plane. (b) To isolate the resonance of choice, we lower the pillar height to its ideal value of  $h_{\text{ideal}} = 1005.7$  nm, separating the resonances from one another. The wavelength range plotted is 1993.2–2007.9 nm. The complex transmission amplitude now draws a circle, allowing us to employ the single-resonance TCMT model. The circle, however, still crosses the origin due to its diffractionless (two-port) nature ( $\lambda/n_{\text{sub}} = 1384.2$ –1394.4 nm), but at the vicinity of the resonance wavelength  $\lambda_0 = 2000.6$  nm ( $\lambda_0/n_{\text{sub}} = 1389.3$  nm), the periodicity of 1387.1 nm is still subwavelength. (c) To expand from the two-port system, we increase the periods in both the  $x$ - and  $y$ -directions ( $P_x = P_y = 1831.8$  nm) to be greater than the wavelength in the substrate (wavelength range: 1962.1–1981.8 nm,  $\lambda/n_{\text{sub}} = 1362.6$ –1376.2 nm). This leads to diffraction within the substrate in both the  $x$ - and  $y$ -directions, making it a six-port system. The complex transmission circle now encircles the origin, leading to a full  $2\pi$  phase revolution, and the black arrow corresponds to the direct scattering parameter  $t_d$ , with the angle defining its argument,  $\arg[t_d] = \theta$ . The resonance wavelength is  $\lambda_0 = 1971.9$  nm. (d) To tune  $\arg[t_d] = \theta$  to the required value of  $\pi$ , we insert a pedestal structure made of LN. The  $x$ -directional width is set to be  $w = 1817.7$  nm and the  $y$ -directional width is set to be equal to the period in the  $y$ -direction,  $P_y = 1831.8$  nm. The thickness of LN is  $t = 263.8$  nm. Tuning the  $w$  and  $P_y$  allows us to tune to  $\arg[t_d] = \theta \approx \pi$ . Notice that the presence of LN increases the quality factor, indicated by the color encoding. The wavelength range is 1996.1–2001.3 nm, with the resonance wavelength being  $\lambda_0 = 1998.7$  nm. (e) To achieve the second required condition of  $t_d = R$ , we change the  $x$ -directional period to  $P_x = 1959.2$  nm, tuning the effective index of the unit cell and the diffraction efficiencies, influencing  $|t_d|$ . The wavelength range is 1995.5–2002 nm, with the resonance wavelength being  $\lambda_0 = 1998.7$  nm. (f) To attain a high quality factor, we make the LN depth thicker to  $t = 339.6$  nm, leading to the circle appearing discrete due to the same wavelength difference becoming further placed apart. The wavelength range is 1999.1–2000.8 nm, with the resonance wavelength being  $\lambda_0 = 2000$  nm. The color information also indicates higher quality factor as the coloring range from red to blue (a fixed wavelength range around the resonance frequency) takes up almost the entire circle, compared to the previous cases.

dynamics are general and do not depend on the specific nature of the single resonance supported by the metasurface.

Note that for all the considered metasurface periods  $P_x$ , the metasurface remains nondiffractive in transmission. This is because the threshold period for diffraction is smaller in the substrate ( $P_0 = \lambda/n_{\text{sub}}$ ) than in air ( $P_0 = \lambda$ ) and the chosen design satisfies  $\lambda_0/n_{\text{sub}} < P_x < \lambda_0$ . Consequently, diffraction channels are open only on the substrate side, while the transmission side remains free of diffraction. The illumination

from the substrate side is intentionally selected to facilitate monolithic integration of the metasurface with on-chip light sources, such as VCSELs or PCSELs.

We note that the moving of the center of the resonance circle on the complex amplitude space so that the resonance circle encircles the origin and thereby have a  $2\pi$  phase revolution, mathematically corresponds to having the branch cut between a pole–zero pair cross through the real frequency axis on the complex frequency space.<sup>21</sup> The equivalence is

shown in Supporting Information, Section 3. Our work therefore proposes a new method of achieving this crossing of the branch cut without using the method of Huygens metasurface with two resonances or explicit time-reversal symmetry breaking.

It is important to note that merely opening the diffraction ports does not ensure that the complex transmission amplitude revolves around the origin. In other words, the presence of additional ports (in our case, diffraction ports) is a necessary—but not a sufficient—condition for achieving a  $2\pi$  phase change in transmission with single resonances, or equivalently  $R > |C|$ .

As briefly discussed above, the complex transmission circle should be “centralized” to enable a phase-only spectral response with constant amplitude. The centralization condition can be written as  $C = R + t_d = 0$ , which is equivalent to two simultaneous conditions  $\arg[t_d] = \pi$  and  $|t_d| = R$ . Here, we propose a design guideline involving a pedestal structure between the high-index Mie resonance pillars and the substrate. Figure 3 illustrates a step-by-step process of our methodology, pairing a specific metasurface setup with the corresponding complex transmission amplitude obtained from full-wave simulations. Figure 3a displays a two-dimensional periodic lattice (in both the  $x$ - and  $y$ -directions) of Ge rectangular pillars on a silica substrate without any diffraction channels. The structure is illuminated from within the substrate by a normally incident  $x$ -polarized wave. This particular geometry hosts three resonances in the vicinity of one another spectrally, and due to the transmission zero phenomenon (no diffraction, two-port system), the complex transmission amplitude passes the origin three times in succession as the wavelength progresses, yielding a ribbon-like curve.

To isolate a single resonance, we altered the pillar geometry. Figure 3b shows the metasurface with reduced height for the pillars so that the complex transmission amplitude draws a circle corresponding to a single resonance. The convention used for the radiative coupling parameters for both the reflective port ( $d_1$ ) and the transmissive port ( $d_2$ ) assumes that they are both positive real-valued. With such a convention, as mentioned above, the leftmost point on the circle corresponds to the direct scattering parameter  $t_d$  (complex-valued) and the rightmost point corresponds to the resonance wavelength. Notice that because it is still a two-port system without diffraction, the circle still possesses a zero near the resonance.

To allow for the encircling of the origin and thereby the  $2\pi$  phase revolution, we open up the diffraction ports by increasing the periodicity in both the  $x$ - and  $y$ -directions. Figure 3c shows the results. It should be noted that because diffraction is also allowed in the  $y$ -direction, we get a six-port system (four diffraction ports, two from the  $x$ - and  $y$ -directions each). By having the condition  $\lambda/n_{\text{sub}} < P_x = P_y < \lambda$ , diffraction is allowed into the substrate but not into the air on the transmission side. This shifts the complex transmission circle slightly closer to the origin, with the scattered phase spanning the full  $0-2\pi$  range as the wavelength evolves around the resonance wavelength. The direct scattering parameter  $t_d$  is depicted with a black arrow, with its argument denoted as  $\arg[t_d] = \theta$ . Despite enabling  $2\pi$  phase variation, the circular trajectory is not ideal, since it does not fulfill  $C = R + t_d = 0$ .

The  $\arg[t_d]$  can be engineered by introducing a pedestal slab between the dielectric pillar and the substrate. The material used for the pedestal in our system is lithium niobate (LN), chosen for its electro-optic tunability. Applying a bias across

the LN can modify its refractive index, which will shift the resonance frequency of the resonance residing in the pillars above and hence modulate the transmitted phase dynamically. We chose the LN slab to be infinitely extended into the  $y$ -direction for the sake of simplicity in the design. The width  $w$  of the LN slab and the periodicity in the  $y$ -direction  $P_y$  (which also determines the  $y$ -directional length of the LN slab per unit cell) can be tuned independently such that  $\arg[t_d]$  either increases or decreases. This is because, in addition to the effective index being altered due to the presence of the LN slab, which affects the direct scattering parameter  $t_d$ , the change in the surrounding refractive index distribution of the Ge pillar modifies the complex radiative coupling parameters of the resonance.<sup>26</sup> Because our phase references are chosen such that  $\arg[d_1] = \arg[d_2] = 0$ , changes in the radiative coupling dynamics are reflected as compensated changes in  $\arg[t_d]$  (see Supporting Information, Section 1). We chose  $w = 1817.7$  nm and  $P_y = 1831.8$  nm. Figure 3d shows the corresponding complex transmission amplitude circle with  $\arg[t_d] \approx \pi$ .

The coloring scheme in the circle plots (3b–3f) illustrates the quality factor information, with a more spread-out rainbow coloring around the resonance point (the point colored dark red with a black outline) implying a higher quality factor (see Supporting Information, Section 4). As well as achieving the desired  $\arg[t_d] \approx \pi$ , one can see that the addition of the LN slab has increased the quality factor of the resonance. The reason for the increase in the quality factor with the addition of the LN is because having a higher-index material (than air or substrate) around a periodic dielectric meta-atom (and therefore have a lower index contrast between the pillar and the environment) tends to decrease the radiative coupling.<sup>37,38</sup> This is opposed to the conventional wisdom that radiative coupling decreases when the index contrast increases for a localized resonator,<sup>39</sup> implying that in our system the periodic array effect is the more significant of the two competing effects.

The circle is still yet to be centralized, as it is shifted to the left from the center. This is because the magnitude of the direct scattering parameter  $|t_d|$  is too large compared to the radius ( $|t_d| > R$ ). To resolve this issue, we tune the period in the  $x$ -direction,  $P_x$ . This has the effect of influencing  $|t_d|$  through two mechanisms: one is the change in the effective index of the unit-cell (air to pillar/LN ratio of the unit cell), which can affect the  $|t_d|$ , and the other is the tuning of the diffraction efficiencies  $\alpha_i$ , which also indirectly affects  $|t_d|$  through energy conservation. It can be seen from the transition from Figure 3d,e that  $|t_d|$  can be tuned through  $P_x$  without affecting  $\arg[t_d]$  significantly. This is because tuning  $P_x$  does not change the size and shape of the LN, which greatly influences  $\arg[t_d]$ . Figure 3e shows a structure with a larger  $P_x = 1959.2$  nm, and the corresponding transmission circle satisfies  $C = R + t_d = 0$ , resulting in a centralized circle.

For our final step in the preparation for active phase-only modulation, we increase the quality factor of the resonance further, as this greatly helps in the sense that the resonance frequency does not have to be tuned as much to cover the  $2\pi$  phase range.<sup>10</sup> Further enhancement of the quality factor is done through making the LN pedestal thicker for the reasons discussed above. Figure 3f shows the final metasurface that has a centralized complex transmission amplitude circle with a high quality factor and has a radius that is almost 0.5, which is the theoretical upper bound. Because the wavelength sampling rate is fixed for Figure 3b–f, the circle is now discretized, as the

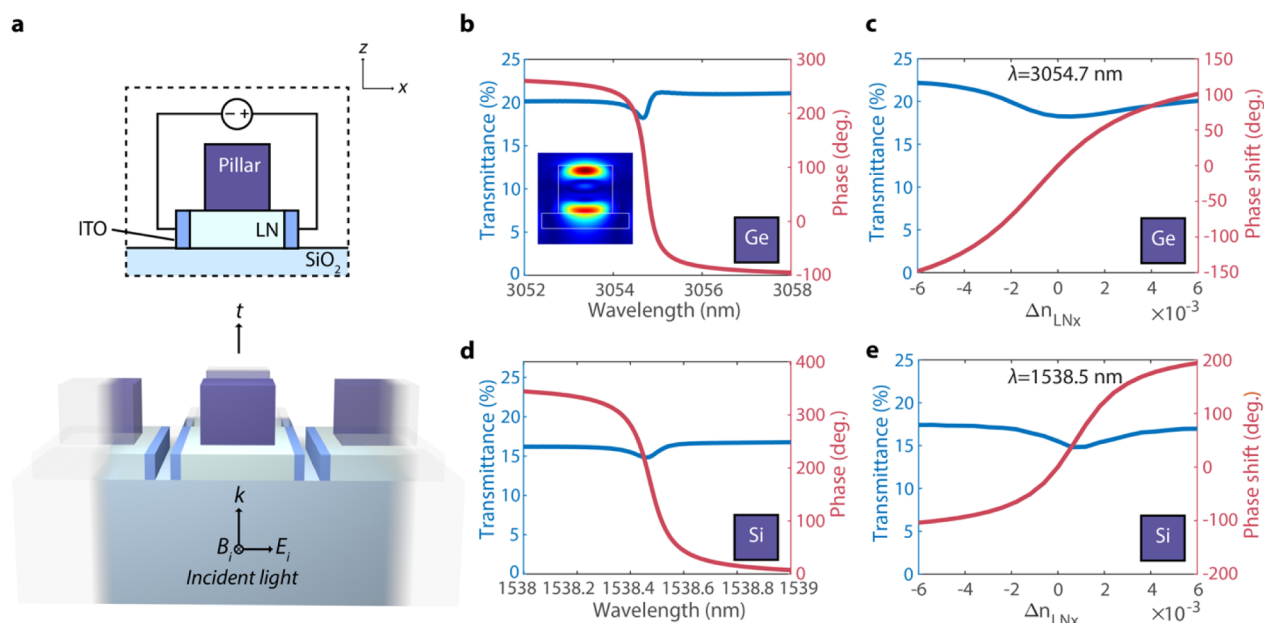


**Figure 4.** Metasurface setup for dynamic phase modulation, **Figure 4.** (a) Our dynamic phase modulation metasurface configuration with ITO electrodes for electro-optically modulating the LN refractive index. The pillars can either be Ge or Si, with the Ge results shown in (b,c), and the Si results shown in (d,e). The dimensions for the Ge configuration are as follows. Ge pillar: 1800 nm  $\times$  1800 nm  $\times$  1540 nm (height),  $P_x$ : 3000 nm,  $P_y$ : 2770 nm, LN width: 2680 nm, LN thickness: 520 nm, ITO width: 40 nm, and ITO thickness: 520 nm. The dimensions for the Si configuration are as follows. Si pillar: 963 nm  $\times$  963 nm  $\times$  830 nm (height),  $P_x$ : 1500 nm,  $P_y$ : 1440 nm, LN width: 1220 nm, LN thickness: 260 nm, ITO width: 40 nm, and ITO thickness: 260 nm. (b) The spectral transmittance and phase for the Ge configuration, with the inset showing the electric field profile in the  $x$ - $z$  plane for the Mie resonance (dotriacontapole) in the pillar. (c) The transmittance and the phase shift with respect to the change of the  $x$ -component of the LN refractive index for the Ge configuration. The operating wavelength is designed to be 3054.7 nm. (d) The spectral transmittance and phase for the Si configuration. (e) The transmittance and phase shift with respect to the change of the  $x$ -component of the LN refractive index for the Si metasurface. The operating wavelength is designed to be 1538.5 nm.

high quality factor results in the circle being swept across rapidly.

**Supporting Information**, Section 4, shows the numerical values of the radii  $R$ , as well as the direct transmission scattering parameters  $t_d$  and the quality factors  $Q$  for the circles shown in **Figure 3**. It can be seen that as the circle progresses from **Figure 3b–f**, the circle radius  $R$  and the quality factor  $Q$  keep increasing. We note that the tuning of only the radius of the circle, given by  $R = \sqrt{\gamma_r \gamma_d} / \gamma$ , was not shown because it was difficult to isolate a geometric variable that only influenced  $R$ . Nonetheless, due to the sufficient number of geometric parameters of our metasurface configuration, we were able to find multiple parameter sets that resulted in a centralized circle, allowing us to select the parameter set that yielded the largest radius  $R$  (see **Supporting Information**, Section 5). So, our methodology includes tuning both the  $t_d$  and  $t_r$  (through the radiative losses in  $t_r$ ) in the complex transmission amplitude  $t = t_d + t_r$  through judiciously tuning the metasurface geometric parameters.

It should also be worth noting that the steps from **Figure 3d–f** can be achieved with other materials with a refractive index higher than the substrate and lower than the pillar, so it is expected that using materials such as barium titanate (BTO) with a higher electrooptic tunability will yield better dynamic modulation performances. Additionally, this methodology utilizing a pedestal is general in the sense that it can shape the direct scattering parameter and tune the quality factor of the resonance for other applications as well, such as creating a critical coupling condition for the purpose of coherent perfect absorption.

Finally, we demonstrate the dynamic phase modulation capability of our metasurface. By introducing ITO electrodes into the metasurface structure and bias-gating the ITO electrodes with respect to each other (**Figure 4a**), the refractive index of the LN slab can be electro-optically modulated through the Pockels effect, leading to shifts in the resonance frequency of the pillar and changes in the phase of the transmitted light. To demonstrate the versatility of our approach, we showcase dynamic transmissive phase-only modulation using two different pillar materials: Ge (as in **Figure 3**) and Si. The Ge metasurface is designed to operate in the mid-IR (infrared) wavelength range, while the Si metasurface operates in the near-IR telecommunication frequencies. As shown in the spectral response of the designed metasurfaces (**Figure 4b,d**), introducing lossy ITO electrodes does not compromise the desired spectral characteristics—namely, near-constant transmittance with a corresponding full phase variation across the spectrum. This robustness is attributed to our design strategy, wherein the electrodes are positioned away from regions experiencing a significant field enhancement.

The electro-optic modulation performance of the Ge and Si metasurfaces are presented in **Figure 4c,e**, respectively. In our simulations, we assume that the  $x$ -component of the LN refractive index can be modulated by up to  $\pm 0.006$  under an applied bias.<sup>40,41</sup> The Ge metasurface achieves a phase shift of 250° while maintaining an almost constant transmittance of 20%. Note that this corresponds to a normalized complex transmission amplitude of 0.45, which is remarkably close to the established theoretical upper bound of 0.5 (**Figure 4c**). The Si-based metasurface, as illustrated in **Figure 4e**, achieves a

phase modulation range of approximately  $300^\circ$  while maintaining a nearly constant transmittance of  $\sim 16\%$  (corresponding to a normalized complex transmission amplitude of  $\sim 0.4$ ).

It is also worth noting that there is an upper bound for the resolution of the meta-atoms of the metasurface, as the period must be larger than the diffraction threshold within the substrate,  $P_x \geq \lambda/n$ . This enables subwavelength wavefront control of the transmitted light, provided that the refractive index on the transmission side is sufficiently low (e.g., air with  $n = 1$ ).

Another important point is that in our simulations, the substrate is treated as optically infinite, allowing diffracted waves to freely propagate into the far field. In practice, however, the substrate is of finite thickness, and without properly engineered outcoupling mechanisms, the diffracted light would remain confined within the substrate due to total internal reflection. Because TCMT mandates that extending the scattered phase beyond the  $0-\pi$  range requires the presence of additional far-field radiative channels, experimental implementations must include controlled outcoupling to free space at positions corresponding to the respective diffraction angles. In cascaded systems where the noise from such additional diffraction channels could be problematic, the outcoupling structures can be designed to exhibit low efficiency, ensuring that while the ports remain open (to satisfy the  $0-2\pi$  phase range condition), the amount of stray optical power coupled out—and hence the potential noise in cascaded systems—remains minimal.

## CONCLUSION

The interference between a resonance and the continuum in systems with an incident port and an output transmission port exhibits a transmission zero in the Fano spectrum. This inherently prevents dynamical phase-only modulation with a full  $2\pi$  phase range in transmissive metasurfaces. We have demonstrated that utilizing additional diffraction ports in reflection effectively bestows additional degrees of freedom in shaping the continuum mode and allows for a complete spectral  $0-2\pi$  phase range in transmission. This is mathematically equivalent to pushing the transmission zero upward in the complex frequency space so that the real frequency axis crosses the branch cut. Also, to allow for phase-only modulation with constant amplitude, we have proposed a generally applicable, step-by-step methodology using a pedestal structure that allows for the tuning of the continuum mode, which can enable dynamic transmissive phase modulation having  $0-2\pi$  phase range with uniform amplitude.

It is important to note that the additional ports used to engineer the direct transmission scattering parameter do not have to be diffraction channels. They can be orthogonal polarization channels, guided surface waves, or any other channel that radiates energy away. Because the TCMT formalism allows lifting the  $R \leq |C|$  constraint by merely adding more ports, we believe that it is possible to engineer the  $t_d$  and the radius of the complex transmission amplitude circle by tuning geometric parameters of metasurfaces with additional ports other than diffraction ports. For example, if we are to use circularly polarized light as incident input (left circular polarization, for example) and have the cross-polarization reflection and transmission as the additional port channels,  $|t_d|$  could be decreased as above by increasing cross-polarization conversion efficiencies, and  $\arg[t_d]$  and the radius of the

transmission amplitude could be adjusted by tuning the radiative losses of the metasurface. Also, the theoretical upper bound of 0.5 in the transmission amplitude could be further elevated by using materials or methods that allow non-reciprocity. We look forward to future research that builds upon our work and improves our performance. Lastly, this methodology can be applied to other photonic applications that require tuning of the continuum mode and quality factors, such as coherent perfect absorbers. We hope that the contents of this paper help pave the way for a wide range of photonic applications that demand ultimate control over light.

## METHODS

Full wave optical simulations are performed using the finite difference time domain method using commercial software (FDTD Lumerical). In our optical simulations, a normally incident linear  $x$ -directionally polarized plane wave illuminates the metasurface from within the substrate (see Figures 2–4). When simulating an array of high-index pillars, periodic boundary conditions are used in the  $x$ - and  $y$ -directions, and a perfectly matched layer (PML) boundary condition is used in the  $z$ -direction. In Figure 2, the mesh override region covers the whole simulation area so that the mesh in the  $x$ -direction is 5 nm, while the mesh in the  $z$ - and  $y$ -directions is set to 20 nm. An additional geometry-based mesh of  $20 \times 20 \times 20$  nm overrides the high-index pillar. In Figure 3, when performing full-wave simulations in Lumerical, we used AutoMesh with mesh accuracy set to 3. In our simulations, the minimal autosutoff level was  $10^{-11}$ . In Figure 4, we introduced geometry-based mesh override regions covering the ITO electrodes such that the mesh in the  $x$ -direction was set to 8 nm, while the mesh in the  $y$ - and  $z$ -directions was set to 20 nm. The geometrical parameters of the metasurface are reported with a subnanometer precision to represent our simulation setup accurately. However, for achieving the target optical behavior, such precision is not needed (for sensitivity analysis, see Supporting Information, Section 12).

In our optical simulation, the refractive index of Ge is set to  $n_{\text{Ge}} = 4$ , the refractive index of Si is set to  $n_{\text{Si}} = 3.734$ , and the refractive index of SiO<sub>2</sub> is taken as 1.44. In Figures 2,3 and 4d,e, the ordinary refractive index of the LNO is  $n_y = n_z = 2.21$ , while the extraordinary refractive index is taken as  $n_x = 2.12$ . In Figure 4b,c, the ordinary refractive index of the LNO is  $n_y = n_z = 2.159$ , while the extraordinary refractive index is taken as  $n_x = 2.095$ .

## ASSOCIATED CONTENT

### Data Availability Statement

All data needed to evaluate the conclusions in the paper are present in the paper and/or the Supporting Information.

### Supporting Information

The Supporting Information is available free of charge at <https://pubs.acs.org/doi/10.1021/acsnano.5c13223>.

TCMT formalism and additional full-wave simulation data (PDF)

## AUTHOR INFORMATION

### Corresponding Authors

Harry A. Atwater – Thomas J. Watson Laboratories of Applied Physics, California Institute of Technology, Pasadena, California 91125, United States; [orcid.org/0000-0001-9435-0201](https://orcid.org/0000-0001-9435-0201); Email: [haa@caltech.edu](mailto:haa@caltech.edu)

Min Seok Jang – Department of Electrical Engineering, Korea Advanced Institute of Science and Technology, Daejeon 34141, South Korea; Thomas J. Watson Laboratories of Applied Physics, California Institute of Technology, Pasadena, California 91125, United States; [orcid.org/0000-0002-5683-1925](https://orcid.org/0000-0002-5683-1925); Email: [jang.minseok@kaist.ac.kr](mailto:jang.minseok@kaist.ac.kr)

## Authors

**Juyoung Kim** – Department of Electrical Engineering, Korea Advanced Institute of Science and Technology, Daejeon 34141, South Korea; Thomas J. Watson Laboratories of Applied Physics, California Institute of Technology, Pasadena, California 91125, United States

**Ruzan Sokhoyan** – Thomas J. Watson Laboratories of Applied Physics, California Institute of Technology, Pasadena, California 91125, United States; [orcid.org/0000-0003-4599-6350](https://orcid.org/0000-0003-4599-6350)

**Minkyoon Yi** – Department of Electrical Engineering, Korea Advanced Institute of Science and Technology, Daejeon 34141, South Korea

**Sangjun Han** – Department of Electrical Engineering, Korea Advanced Institute of Science and Technology, Daejeon 34141, South Korea; Department of Mechanical Engineering, University of California, Berkeley, California 94720, United States

Complete contact information is available at:  
<https://pubs.acs.org/10.1021/acsnano.5c13223>

## Author Contributions

J.K. and R.S. contributed equally. J.K., R.S., and M.S.J. conceived and designed the research. J.K. and M.S.J. established the theoretical framework. J.K., R.S., M.Y., and S.H. performed simulations and analyzed the data. R.S. designed the proof-of-concept metasurface configuration. J.K. visualized the data, with R.S., H.A.A., and M.S.J. assisting. H.A.A. and M.S.J. supervised the process. J.K. wrote the original draft, and R.S., H.A.A., and M.S.J. reviewed and edited it.

## Funding

This research was supported by the National Research Foundation of Korea (NRF) grants funded by the Ministry of Science and ICT (RS-2024-00414119, RS-2024-00416583), and by the Meta-Imaging MURI grant #FA9550-21-1-0312 from Air Force Office of Scientific Research. The authors also acknowledge support from the President's and Director's Research Development Fund (PDRDF-2022-046). This work was partly supported by the Institute of Information and Communications Technology Planning and Evaluation (IITP) grant funded by the Korea government (MSIT) (RS-2024-00412644) and by the Culture, Sports and Tourism R&D Program through the Korea Creative Content Agency grant funded by the Ministry of Culture, Sports and Tourism in 2024 (RS-2024-00332210). The authors gratefully acknowledge useful discussions with Jared Sisler.

## Notes

This work has been submitted to the Research Square preprint server under: Kim et al., 2025. Ju Young Kim; Ruzan Sokhoyan; Minkyoon Yi; Sangjun Han; Harry Atwater; Minseok Jang; Overcoming Barriers to Dynamic Phase-only Modulation in Transmissive Metasurfaces via Diffraction Control. 2025, rs-6989280. Research Square. [10.21203/rs.3.rs-6989280/v1](https://doi.org/10.21203/rs.3.rs-6989280/v1) (accessed January 22, 2026).

The authors declare no competing financial interest.

## REFERENCES

(1) Kim, I.; Martins, R. J.; Jang, J.; Badloe, T.; Khadir, S.; Jung, H.; Kim, H.; Kim, J.; Genevet, P.; Rho, J. Nanophotonics for light

detection and ranging technology. *Nat. Nanotechnol.* **2021**, *16*, 508–524.

(2) Juliano Martins, R.; Marinov, E.; Youssef, M. A. B.; Kyrou, C.; Joubert, M.; Colmagro, C.; Gâté, V.; Turbil, C.; Coulon, P.; Turover, D.; Khadir, S.; Giudici, M.; Klitis, C.; Sorel, M.; Genevet, P. Metasurface-enhanced light detection and ranging technology. *Nat. Commun.* **2022**, *13*, 5724.

(3) He, S.; Wang, R.; Luo, H. Computing metasurfaces for all-optical image processing: a brief review. *Nanophotonics* **2022**, *11* (6), 1083–1108.

(4) Aththanayake, A.; Lininger, A.; Strangi, C.; Griswold, M. A.; Strangi, G. Tunable holographic metasurfaces for augmented and virtual reality. *Nanophotonics* **2025**, *14*, 3813.

(5) Gao, H.; Wang, Y.; Fan, X.; Jiao, B.; Li, T.; Shang, C.; Zeng, C.; Deng, L.; Xiong, W.; Xia, J.; Hong, M. Dynamic 3D meta-holography in visible range with large frame number and high frame rate. *Sci. Adv.* **2020**, *6*, No. eaba8595.

(6) Yu, N.; Genevet, P.; Kats, M. A.; Aieta, F.; Tetienne, J. P.; Capasso, F.; Gaburro, Z. Light propagation with phase discontinuities: generalized laws of reflection and refraction. *Science* **2011**, *334*, 333–337.

(7) Hail, C. U.; Foley, M.; Sokhoyan, R.; Michaeli, L.; Atwater, H. A. High quality factor metasurfaces for two-dimensional wavefront manipulation. *Nat. Commun.* **2023**, *14*, 8476.

(8) Brongersma, M. L.; Pala, R. A.; Altug, H.; Capasso, F.; Chen, W. T.; Majumdar, A.; Atwater, H. A. The second optical metasurface revolution: moving from science to technology. *Nat. Rev. Electr. Eng.* **2025**, *2*, 125–143.

(9) Kuznetsov, A. I.; Brongersma, M. L.; Yao, J.; Chen, M. K.; Levy, U.; Tsai, D. P.; Zheludev, N. I.; Faraon, A.; Arbabi, A.; Yu, N.; Chanda, J.; Crozier, K. B.; Kildishev, A. V.; Wang, H.; Yang, J. K. W.; Valentine, J. G.; Genevet, P.; Fan, J. A.; Miller, O. D.; Majumdar, A.; Fröch, J. E.; Brady, D.; Heide, F.; Veeraraghavan, A.; Engheta, N.; Alù, A.; Polman, A.; Atwater, H. A.; Thureja, P.; Paniagua-Dominguez, R.; Ha, S.; Barreda, A. I.; Schuller, J. A.; Staude, I.; Grinblat, G.; Kivshar, Y.; Peana, S.; Yelin, S. F.; Senichev, A.; Shalaev, V. M.; Saha, S.; Boltasseva, A.; Rho, J.; Oh, D.; Kim, J.; Park, J.; Devlin, R.; Pala, R. A. Roadmap for optical metasurfaces. *ACS Photonics* **2024**, *11*, 816–865.

(10) Kim, J. Y.; Park, J.; Holdman, G. R.; Heiden, J. T.; Kim, S.; Brar, V. W.; Jang, M. S. Full  $2\pi$  tunable phase modulation using avoided crossing of resonances. *Nat. Commun.* **2022**, *13*, 2103.

(11) Han, S.; Kong, J.; Choi, J.; Chegal, W.; Jang, M. S. Single-gate electro-optic beam switching metasurfaces. *Light Sci. Appl.* **2025**, *14* (1), 292.

(12) Park, J.; Kim, J. Y.; Nam, S.; Jang, M. S. High-directivity multi-level beam switching with single-gate tunable metasurfaces based on graphene. *Adv. Opt. Mater.* **2025**, *13*, 2500236.

(13) Solntsev, A. S.; Agarwal, G. S.; Kivshar, Y. S. Metasurfaces for quantum photonics. *Nat. Photonics* **2021**, *15*, 327–336.

(14) Neshev, D. N.; Miroshnichenko, A. E. Enabling smart vision with metasurfaces. *Nat. Photonics* **2023**, *17*, 26–35.

(15) Park, J.; Kang, J. H.; Liu, X.; Maddox, S. J.; Tang, K.; McIntyre, P. C.; Bank, S. R.; Brongersma, M. L. Dynamic thermal emission control with InAs-based plasmonic metasurfaces. *Sci. Adv.* **2018**, *4*, No. eaat3163.

(16) Park, J.; Kang, J. H.; Kim, S. J.; Liu, X.; Brongersma, M. L. Dynamic reflection phase and polarization control in metasurfaces. *Nano Lett.* **2017**, *17*, 407–413.

(17) Lynch, J.; Kumar, P.; Chen, C.; Trainor, N.; Kumari, S.; Peng, T. Y.; Chen, C. Y.; Lu, Y.; Redwing, J.; Jariwala, D. Full  $2\pi$  phase modulation using exciton-polaritons in a two-dimensional superlattice. *Device* **2025**, *3*, 100639.

(18) Yoshida, M.; Katsuno, S.; Inoue, T.; Gellela, J.; Izumi, K.; De Zoysa, M.; Ishizaki, K.; Noda, S. High-brightness scalable continuous-wave single-mode photonic-crystal laser. *Nature* **2023**, *618*, 727–732.

(19) Xiao, Y.; Wang, J.; Liu, H.; Miao, P.; Gou, Y.; Zhang, Z.; Deng, G.; Zhou, S. Multi-junction cascaded vertical-cavity surface-emitting laser with a high power conversion efficiency of 74%. *Light Sci. Appl.* **2024**, *13*, 60.

- (20) Sun, S.; Yang, K.; Wang, C.; Juan, T.; Chen, W.; Liao, C.; He, Q.; Xiao, S.; Kung, W.; Guo, G.; Zhou, L.; Tsai, D. P. High-Efficiency Broadband Anomalous Reflection by Gradient Meta-Surfaces. *Nano Lett.* **2012**, *12*, 6223–6229.
- (21) Colom, R.; Mikheeva, E.; Achouri, K.; Zuniga-Perez, J.; Bonod, N.; Martin, O. J.; Burger, S.; Genevet, P. Crossing of the Branch Cut: The Topological Origin of a Universal  $2\pi$ -Phase Retardation in Non-Hermitian Metasurfaces. *Laser Photonics Rev.* **2023**, *17*, 2200976.
- (22) Mikheeva, E.; Colom, R.; Achouri, K.; Overvig, A.; Binkowski, F.; Duboz, J. Y.; Cuffe, S.; Fan, S.; Burger, S.; Alù, A.; et al. Asymmetric phase modulation of light with parity-symmetry broken metasurfaces. *Optica* **2023**, *10*, 1287–1294.
- (23) Wang, K. W.; Yu, Z.; Sandhu, S.; Fan, S. Fundamental bounds on decay rates in asymmetric single-mode optical resonators. *Opt. Lett.* **2013**, *38*, 100–102.
- (24) Epstein, A.; Eleftheriades, G. V. Huygens' metasurfaces via the equivalence principle: design and applications. *JOSA B* **2016**, *33*, A31–A50.
- (25) Mikheeva, E.; Colom, R.; Genevet, P.; Bedu, F.; Ozerov, I.; Khadir, S.; Baffou, G.; Abdeddaim, R.; Enoch, S.; Lumeau, J. Uniform Huygens Metasurfaces with Postfabrication Phase Pattern Recording Functionality. *ACS Photonics* **2023**, *10*, 1538–1546.
- (26) Ollanik, A. J.; Smith, J. A.; Belue, M. J.; Escarra, M. D. High-efficiency all-dielectric Huygens metasurfaces from the ultraviolet to the infrared. *ACS Photonics* **2018**, *5*, 1351–1358.
- (27) Decker, M.; Staude, I.; Falkner, M.; Dominguez, J.; Neshev, D. N.; Brener, I.; Pertsch, T.; Kivshar, Y. S. High-efficiency dielectric Huygens' surfaces. *Adv. Opt. Mater.* **2015**, *3*, 813–820.
- (28) Liu, M.; Choi, D. Y. Extreme Huygens' metasurfaces based on quasi-bound states in the continuum. *Nano Lett.* **2018**, *18*, 8062–8069.
- (29) Yang, Z.; Liu, M.; Komar, A.; Xu, L.; Neshev, D. N. Phase-only tuning of extreme Huygens metasurfaces enabled by optical anisotropy. *Adv. Opt. Mater.* **2022**, *10*, 2101893.
- (30) Huang, S. H.; Su, H. P.; Chen, C. Y.; Lin, Y. C.; Yang, Z.; Shi, Y.; Song, Q.; Wu, P. C. Microcavity-assisted multi-resonant metasurfaces enabling versatile wavefront engineering. *Nat. Commun.* **2024**, *15* (1), 9658.
- (31) Faraz, F.; Tian, J.; Abbasi, T. U.; Zhu, W. Recent advances in geometric phase metasurfaces: Principles and applications. *Adv. Phys. Res.* **2025**, *4* (2), 2400095.
- (32) Ahmed, H.; Rahim, A. A.; Maab, H.; Ali, M. M.; Mahmood, N.; Naureen, S. Phase engineering with all-dielectric metasurfaces for focused-optical-vortex (FOV) beams with high cross-polarization efficiency. *Opt. Mater. Express* **2020**, *10*, 434–448.
- (33) Zhang, Z.; Wang, F.; Wang, H.; Hu, Y.; Yin, X.; Hu, W.; Peng, C. All-pass phase shifting enabled by symmetric topological unidirectional guided resonances. *Opt. Lett.* **2022**, *47* (11), 2875–2878.
- (34) Lee, K. Y.; Yoo, K. W.; Monticone, F.; Yoon, J. W. Dirac bilayer metasurfaces as an inverse Gires-Tournois etalon. *Phys. Rev. Res.* **2025**, *7* (4), 043067.
- (35) Choi, D.; Lee, K. Y.; Shin, D. J.; Yoon, J. W.; Gong, S. H. Unidirectional guided resonance continuum of Dirac bands in WS<sub>2</sub> bilayer metasurfaces. *Nat. Nanotechnol.* **2025**, *20*, 1026–1033.
- (36) Sokhoyan, R.; Hail, C. U.; Foley, M.; Grajower, M. Y.; Atwater, H. A. All-Dielectric High-Q Dynamically Tunable Transmissive Metasurfaces. *Laser Photonics Rev.* **2024**, *18*, 2300980.
- (37) Rosenblatt, D.; Sharon, A.; Friesem, A. A. Resonant grating waveguide structures. *IEEE J. Quantum Electron.* **1997**, *33*, 2038–2059.
- (38) Yildirim, D. U.; Ghobadi, A.; Soydan, M. C.; Gokbayrak, M.; Toprak, A.; Butun, B.; Ozbay, E. Colorimetric and near-absolute polarization-insensitive refractive-index sensing in all-dielectric guided-mode resonance based metasurface. *J. Phys. Chem. C* **2019**, *123*, 19125–19134.
- (39) Van de Groep, J.; Polman, A. Designing dielectric resonators on substrates: Combining magnetic and electric resonances. *Opt. Express* **2013**, *21*, 26285–26302.
- (40) Thomaschewski, M.; Zenin, V. A.; Wolff, C.; Bozhevolnyi, S. I. Plasmonic monolithic lithium niobate directional coupler switches. *Nat. Commun.* **2020**, *11*, 748.
- (41) Thomaschewski, M.; Bozhevolnyi, S. I. Pockels modulation in integrated nanophotonics. *Appl. Phys. Rev.* **2022**, *9*, 021311.



CAS BIOFINDER DISCOVERY PLATFORM™

**ELIMINATE DATA SILOS. FIND WHAT YOU NEED, WHEN YOU NEED IT.**

A single platform for relevant, high-quality biological and toxicology research

**Streamline your R&D**

**CAS**  
A Division of the American Chemical Society